ACS APPLIED NANO MATERIALS

www.acsanm.org
Article

Microfluidic-Assisted Coating of Nanoparticles by Membranes from Extracellular Vesicles

Pablo Alonso-Campos, Francisco Balas, Jose L. Hueso, Víctor Sebastián,* María Sancho-Albero,* and Jesus Santamaría

Cite This: https://doi.org/10.1021/acsanm.5c05265

ABSTRACT: Extracellular vesicle (EV)-based nanotherapies represent a promising alternative in cancer nanomedicine thanks to their targeting properties. However, two major issues remain when combining nanoparticles (NPs) with EVs: (1) safety concerns of cancer-derived EVs related to their oncogenic nature and (2) lack of robust, reproducible, and efficient strategies for NPs coating with EVs membranes. To overcome these main challenges, in this study, we have combined a microfluidic platform to direct the reassembly of previously isolated EVs-derived membranes from lung cancer cells onto fluorescent silica NPs (FSNs). These FSNs leverage the versatile surface functionalization of silica NPs together with intrinsic fluorescent properties for precise intracellular tracking of our hybrids, avoiding membrane-labeling fluorescent probes. While preserving the tumor-targeting properties of natural lung cancer-derived EVs, the proposed microfluidic strategy offers superior handling and manipulation of the process to guarantee (1) homogeneous EV-like coating (6.3 nm thick), (2) high reproducibility, (3) efficient coating yields (87.8% of the NPs were coated), and (4) selective tumor-targeting properties (8.0- and 4.3-fold increases for parental A549 tumoral cells compared to HeLa and fibroblasts at 4 h, respectively). This technology enables the fabrication of biomimetic hybrid core−shell structures with high precision and stability in a continuous process that is more amenable to scaling up.

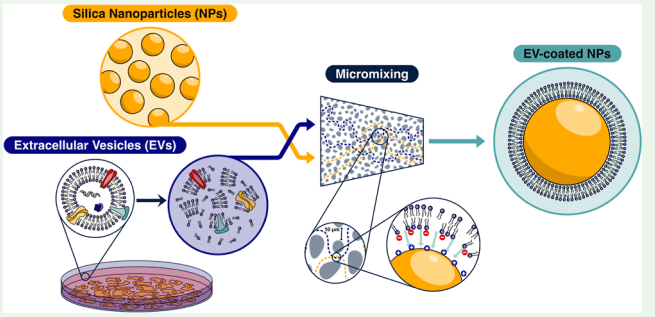

KEYWORDS: *extracellular vesicles, microfluidics, nanoparticles, biomimetics, membrane assembling*

INTRODUCTION

Nanomedicine has raised strong hopes as a promising alternative to improve the lack of selectivity found in conventional chemotherapy, leading to the insufficient accumulation of therapeutic drugs in the tumoral tissues[1] and the often devastating side effects caused by off-target drug delivery. In response to this problem, hundreds of cancer nanomedicines were developed and tried (around 200 cancer nanomedicines were tested in clinical trials by 2019).[2] However, most failed[3,4] due to the same reasons that limit the efficiency of chemotherapy: lack of selective delivery to the tumor. When systemically administered, NPs can accumulate in tumoral cells via passive, i.e., enhanced permeability and retention (EPR) effect, and active targeting routes, i.e., decorating the nanoparticles with targeting agents such as antibodies or peptides. However, as Wilhelm et al. showed nearly a decade ago[5] that, regardless of the targeting (active or passive) method used or the nature of the nanoparticles employed, less than 1% of the delivered dose reaches the tumor and most NPs end up in nontargeted tissues such as liver and spleen as a consequence of recognition and uptake by macrophages.

In recent years, extracellular vesicles (EVs) have been heralded as a way to reduce macrophage uptake and at the same time improve tumor targeting. In fact, in the previous works of our laboratory, we have shown that, by simply encapsulating our NPs in tumor-targeting EVs, their biodistribution improves considerably with respect to the EPR effect.[6,7] However, these works used either an endogenous approach (incubation method,[6] a slow process that cannot guarantee homogeneous loading in the resulting EVs) or the in situ approach based on assembling NPs by a CO reduction method,[7] that can only be applied to noble-metal nanoparticles. It would be much more desirable to have a general methodology able to encapsulate any nanoparticle in EVs membranes, in a fast, scalable, and reproducible way.

The high potential of EVs in targeting is attributed to the fact that cancer-derived EVs exhibit distinct fingerprint features

Received: November 17, 2025
Revised: February 25, 2026
Accepted: March 2, 2026

https://doi.org/10.1021/acsanm.5c05265
ACS Appl. Nano Mater. XXXX, XXX, XXX−XXX

linked to the composition of their membranes, that enable preferential tropism toward their source cells.[8] From this point of view, using EVs produced by tumor cells would appear as the best way to achieve selective delivery of nanomedicines to cancer cells, and in fact, cancer-derived EVs have demonstrated tropism toward the same tumor cell lines.[8] However, the use of tumor EVs as delivery vectors presents a strong limitation: because of their biological content, they have been found to be key mediators in premetastatic niche formation, angiogenesis, and tumor progression.[9,10] To overcome this problem, some authors have proposed using only EVs membranes while avoiding their biological contents. EV target-recognition properties reside on their membrane, where both protein (tetraspanins, integrins, protein glycosylation patters, etc.) and lipid signatures are crucial for target cell recognition and uptake.[11,12] Harnessing these cancer-EV membrane molecular patterns while discarding their internal protumoral cargo is essential for safe and specific EV-based therapies. Different methods have been studied to empty tumor EVs and then harvest their membranes, that, in a subsequent stage, are combined with the desired therapy (e.g., RNA,[13] siRNA,[14] or NPs[15−17]) to create fully artificial EVs-like vectors for selective delivery to cancer cells. In the case of therapeutic NPs, the NP itself can be used as a template and the surface can be functionalized to reconstruct the EVs membrane around itself.

However, coating therapeutic vectors with EVs and maintaining a level of functionality similar to that of the pristine EVs are highly challenging. Among the main problems are reproducing the original pattern of membrane proteins and their distribution over the vector (e.g., a NP) as a homogeneous coating, with good reproducibility. It would also be desirable to devise continuous coating processes as these are more easily scaled up. Before these artificial vectors can be widely employed, methods to produce them reliably in large amounts will be required.

Microfluidics enables precise control and manipulation of fluids at the nano- and microscales, and has therefore been used to achieve scalable, homogeneous, and reproducible synthesis of nanomaterials.[18,19] These microfluidic-assisted NP syntheses encompass both inorganic and organic nanostructures[19,20] including noble metal NPs (e.g., plasmonic hollow gold nanoparticles[21] and gold nanorods[22]), metal oxide NPs (e.g., mesoporous silica nanofibers,[23] iron oxide,[24] and bismuth oxide NPs[25]), quantum dots,[26] liposomes (with special relevance for drug delivery[27]), and polymer NPs (e.g., PLGA[28]). Regarding scalability, microfluidics can overcome this challenge using multiple methods: by increasing the diameter and length of channels,[21] through parallelization of microfluidic devices,[29] or by micromixer geometry modeling and refinement,[30] among many others. Microfluidics also provides new approaches for NP manufacturing with high reproducibility; this homogeneity is achieved by a precise control of the microscale phenomena through passive internal recirculation (in droplet and segmented-based methods[31]), passive mixing mechanisms (hydrodynamic flow focusing, microvortices, and chaotic advection[18]), or active mixing methods (acoustic, electrical, thermal, and pressure mixing[32]). This excellent control offered by microfluidic systems extends beyond single-phase fluids, also enabling superior dispersion of immiscible liquids. For instance, where it is necessary to bring an aqueous and an organic phase into contact to facilitate micelle formation, microfluidic systems represent an excellent choice, promoting processes like emulsification.[33] Also, microfluidic platforms have emerged as powerful tools for the controlled assembly of core−shell and hybrid NPs.[34−36] Liu et al.[37] reported the use of microfluidic sonication to encapsulate NPs within natural EVs or cancer cell membranes coatings. To this end, the core PLGA nanoparticles and either exosomes or cancer cell membranes were fed into a microfluidic system where an intense ultrasound field (80 kHz frequency, 100 W power) could be applied. The compressive pressure generated by microfluidic sonication led to the coating of membranes onto the PLGA cores.[37] In our laboratory, we used microfluidics to assemble surfactant-based vesicles, known as niosomes, in a continuous and scalable manner by harnessing shear stress generated within an interdigital micromixer.[33] This shear-driven assembly was shown to be essential to achieve homogeneity, narrow size distribution, and high reproducibility, overcoming the limitations of conventional batch-based hydration methods.[33] We hypothesized that the efficient micromixing achieved by this platform could be sufficient to achieve a homogeneous coating of EVs membranes on preformed nanoparticles without the need for high intensity ultrasound.

In this study, we have adapted the methodology to direct the assembly of isolated EVs-derived membranes onto silica NPs, using highly efficient mixing enabled by microfluidic technology to allow the continuous preparation of biomimetic hybrid structures with high precision and stability. Previous studies have been successful in the manufacturing of NP-EV hybrids by using microfluidics. Cardellini et al. encapsulated polymeric NPs in liposomes and in whole human embryonic kidney cell-derived whole EVs using a μSonicator.[38] Pareja-Tello et al. recently developed a microfluidic system to encapsulate mRNA in mesenchymal stem cell EVs-lipid hybrid nanoparticles.[39] Also, metal−organic-frameworks (MOFs), core−shell silica-SPIONs structures, or polymeric NPs have been coated with membranes by microfluidics.[37,40−42]

However, these existing microfluidic approaches typically use whole cancer-derived EVs, often overlooking the risks associated with the codelivery of oncogenic cargo. Here, we address this limitation by selectively isolating EV membranes through organic phase extraction, effectively decoupling the lipid bilayer from the hydrophilic intraluminal contents. By utilizing a micromixer to optimize the interfacial assembly between the lipid phase and an aqueous NP phase, we synthesized biomimetic EV-NP hybrids. These biohybrids exhibited high batch-to-batch reproducibility regarding NPs' physicochemical properties, significantly reduced nonspecific uptake, and enhanced tumor targeting against specific (parental) cell lines.

MATERIALS AND METHODS

Synthesis and Functionalization of Fluorescent Silica Nanoparticles

As a template for the coating with EVs membranes, fluorescent silica NPs (FSNs) were prepared. The fluorescent core allowed for an easy monitorization of NP internalization, and their high contrast, together with homogeneous size and good dispersion, contributed to an easy identification and characterization of the membrane layer. FSNs containing fluorescein-5-isothiocyanate (FITC) were synthesized following a previously published and slightly modified protocol (based on the formation of a reverse microemulsion to control the monodispersity and the dimensions of the generated NPs);[43,44] the synthesis steps are shown in Figure S1. Briefly, 5.7 mg of FITC isothiocyanate (in 1 mL of ethanol) was mixed with 73 μL of 3-

https://doi.org/10.1021/acsanm.5c05265
ACS Appl. Nano Mater. XXXX, XXX, XXX−XXX

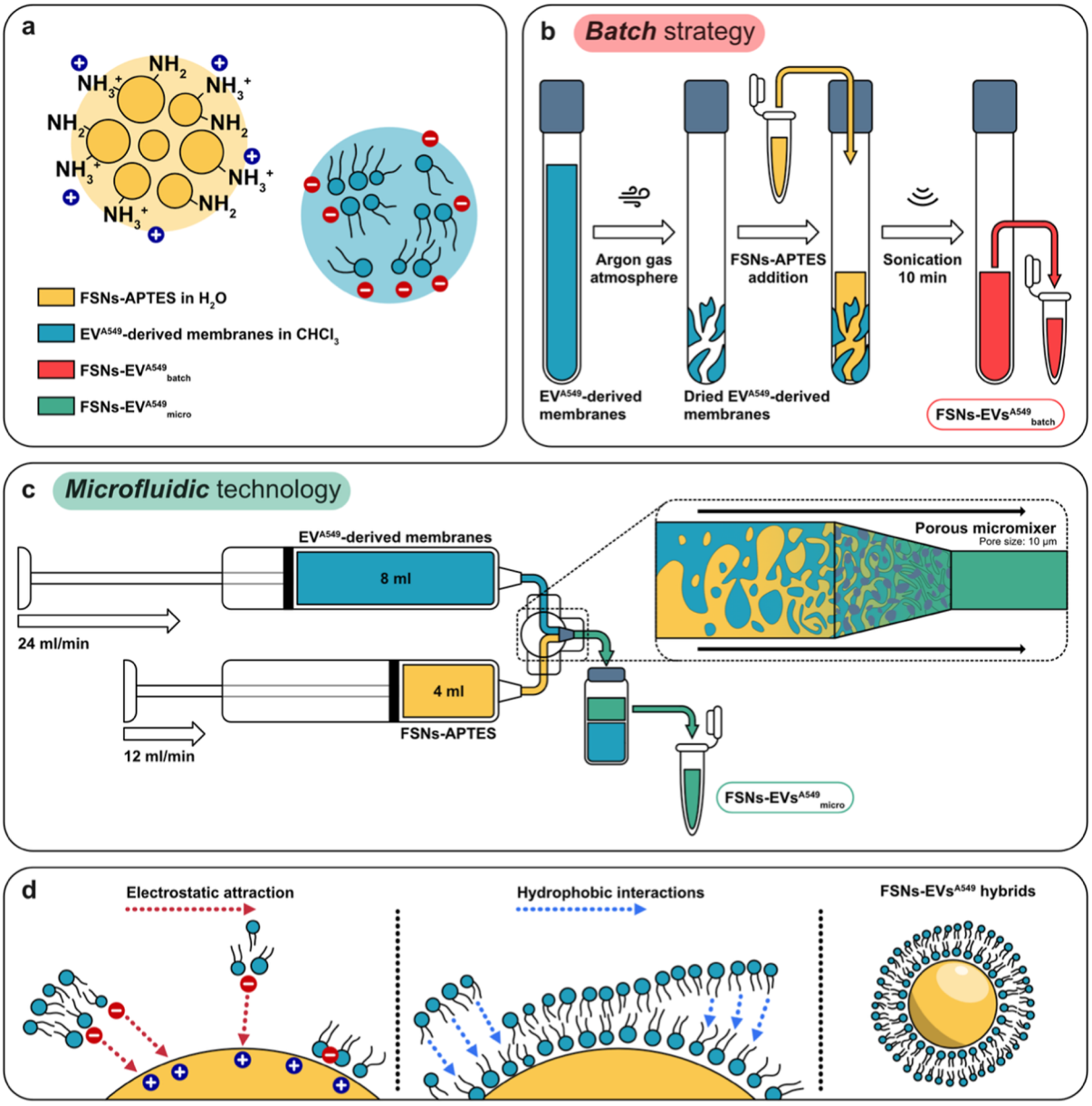

Figure 1. Schematic representation of strategies employed for the generation of the of NPs-EVs^{A549} biohybrids using (a) APTES-functionalized silica nanoparticles and membranes from EVs isolated from A549 cell cultures. (b) In the batch process, the membranes are first dried and deposited over a receiving surface, then brought into contact with a solution that contains FSNs-APTES. The membranes are rehydrated and subjected to ultrasounds to promote their self-assembly around the positively charged NPs. (c) In the microfluidics process, a micromixer is used to provide multiple intimate contact surfaces between two immiscible streams containing the positively charged and the membrane fragments. (d) Both batch and microfluidics NP-coating processes are enabled by electrostatic forces between opposite charges and hydrophobic interactions between the phospholipids' hydrophobic aliphatic chains.

aminopropyltriethoxysilane (APTES) to generate a FITC-APTES conjugate by a bond between the isothiocyanate group (−N═C═S) and the amine groups from the FITC and the APTES, respectively. The solution was stirred under an inert Ar atmosphere at 25 °C for 12 h. Then, 7.7 mL of cyclohexane, 1.6 mL of 1-hexanol, 1.7 mL of Triton X-100, and 0.34 mL of Milli-Q H_2O were mixed during 15 min. Afterward, 100 μL of the prepared FITC-APTES conjugate was gradually added to the previous solution. After 10 min of continuous stirring, 100 μL of tetraethyl orthosilicate (TEOS) were added followed by 100 μL of NH_4OH and 15 μL of 3-(trihydroxysilyl)-propyl methylphosphonate (THPMP) in 10 min time increments. The final solution was kept under stirring at 25 °C for 24 h. After 24 h, 25 mL of EtOH:PrOH:MeOH:H_2O (86:5:5:4, *v:v:v:v*) was added and the synthesized FSNs were washed by centrifugation three times (10,000*g*, 10 min) and stored in EtOH at RT until use.

To achieve a positive surface charge in the FSNs that facilitated assembly of the negatively charged membrane fragments, fluorescent SiO_2-based FSNs were functionalized with APTES as published elsewhere. Briefly, a mass of 1 mg of FSNs was suspended in 1.5 mL of toluene and subsequently mixed with 30 μL of APTES. This solution was stirred for 12 h at 80 °C and then suspended NPs were washed with EtOH (10,000*g*, 10 min) to obtain the purified positively charged FSNs-APTES. Silica NPs (SNs) without any fluorophore were also synthesized for flow cytometry experiments to analyze the expression of the EVs-associated membrane markers assembled on the SN surface. The synthesis of these materials was performed by the Synthesis of Nanoparticles Unit (Unit 9) of the ICTS "NANBIOSIS" at the *Instituto de Nanociencia y Materiales de Aragón* (INMA)-Universidad de Zaragoza.

https://doi.org/10.1021/acsanm.5c05265
ACS Appl. Nano Mater. XXXX, XXX, XXX−XXX

Cell Culture Conditions and Biocompatibility Tests

The A549 cells, HeLa cells, and fibroblasts were cultured in Dulbecco's modified Eagle medium (DMEM) supplemented with 1% penicillin/streptomycin, 1% amphotericin, and 10% fetal bovine serum (FBS). Cell cultures were monitored monthly for mycoplasma before use. For EVs isolation, ultracentrifuged serum (100,000*g*, 2 h, 4 °C) was employed to guarantee EVs-free medium.

The Blue cell viability assay kit (Abnova, USA) was employed to evaluate the cell viability of A549 cells under the effect of FSNs and FSNs-APTES. During the evaluation, A549 cells were seeded into 96-well culture plates at a concentration of 5×10^3 cells/well in 100 μL of the above-mentioned cell culture media. After incubation during 24 h, the medium was changed to 100 μL of freshly prepared medium enriched with FSNs and FSNs-APTES (at concentrations 1, 0.5, 0.25, 0.125, 0.06, 0.03, and 0.016 mg/mL), and cells were cultured for another 24, 48, and 72 h. At these different time points, cells were washed with PBS and then treated with 10% (v/v) of the kit reagent prepared in the conditioned medium following manufacturer instructions. Finally, fluorescence was evaluated at 530/590 nm excitation/emission wavelengths using a Synergy HT (Biotek) plate reader.

EVs Isolation

EVs were collected and purified by successive ultracentrifugation cycles from supernatants of cell culture at 80% confluence.[45] Briefly, cells were seeded and incubated with EVs-free culture media for 48 h. Afterward, their supernatants were collected and centrifuged (2000*g*, 20 min, 4 °C) to discard cell fragments and debris. Then, samples were centrifuged (10,000*g*, 30 min, 4 °C) to eliminate microvesicles, and finally, EVs were isolated by ultracentrifugation (100,000*g*, 2 h, 4 °C) using a Beckman Coulter Optima XE-90 Ultracentrifuge. The resulting EVs pellets were finally washed with PBS to eliminate the contaminants. The final A549-derived EVs (hereafter EVs^{A549}) pellet was suspended in PBS and their concentration was obtained in terms of total protein amount obtained by Pierce protein BCA assay (Thermo-Fisher Scientific, USA).

Characterization Techniques

FSNs, FSNs-APTES, and SNs were characterized by Transmission Electron Microscopy (TEM), Nanoparticle Tracking Analysis (NTA), and zeta potential. For electron microscopy analysis, a FEI TECNAI T20 instrument (Tecnai, Eindhoven, The Netherlands) operated at an accelerating voltage of 200 kV with a LaB_6 electron source fitted with a SuperTwin objective lens, allowing a point-to-point resolution of 2.4 Å, was employed. For evaluating the hydrodynamic diameter of the FSNs and FSNs-APTES, Nanoparticle Tracking Analysis (NTA, Nanosight NS300, Malvern Panalytical) was used. The surface charge of the synthesized materials was analyzed by determining their ζ-potential using Dynamic Light Scattering (DLS) at pH 7 using a Brookhaven 90 Plus equipment using the ZetaPals software. Also, attenuated total reflectance Fourier-Transform Infrared (ATR-FTIR) spectra were recorded on a Bruker Vertex 70 instrument equipped with a DTGS detector in the 600−4000 cm^{-1} spectral region at 4 cm^{-1} resolution.

The morphology, shape, dimensions, and surface charge of the isolated EVs^{A549} were characterized by TEM, NTA, and ζ-potential as previously described. For TEM analysis, an aqueous 3%-phosphotungstic acid (PTA) solution was used as contrast agent. The EVs-associated biomarkers were evaluated by flow cytometry using the MACSPlex Exosome Kit, human (Miltenyi Biotec) following manufacturer instructions.

EVs^{A549} Membrane Isolation and Procedures Used for FSNs Coating: Discontinuous vs Microfluidic Approaches

Figure 1 schematizes the two explored strategies for the assembly of EVs^{A549}-derived membranes around the NPs core.

For both strategies, EVs^{A549}-derived membranes were extracted using a modified Folch extraction approach, as recently reported.[17] Briefly, EVs^{A549} were suspended in a mixture of chloroform, methanol, and PBS ($CHCl_3$:CH_3OH:PBS 8:4:3, *v/v/v*). Then, samples were vigorously vortexed at RT during 10 min before being centrifuged at 6000*g* for 10 min. A biphasic mixture separated by an interface was formed, and the bottom part (containing the organic phase with the hydrophobic EVs components) was extracted with a glass pipet.

In the discontinuous batch strategy, 4 mg of isolated EVs^{A549} membranes were dried under an argon gas atmosphere to avoid membrane oxidation and were stored at −20 °C until used. The so-obtained EVs^{A549} membrane blocks were hydrated by directly adding 2 mg of FSNs-APTES (0.5 mg/mL in water) to allow their spontaneous assembly on the NP surface (ratio FSNs-APTES:EVs^{A549} 1:2, *w/w*). This mixture was finally sonicated for 10 min in an ultrasonic bath to obtain the EVs^{A549}-coated FSNs by using the discontinuous approach (FSNs-$EVs^{A549}{}_{batch}$).

Building upon our previous work[46] on achieving efficient mixing in immiscible fluid microflows using different flow junctions as micromixers, here, we emphasize the importance of controlled stream distribution for promoting the reproducible assembly of nanostructures. For this microfluidic assembly, 2 mg of FSNs-APTES was resuspended in 4 mL of Milli-Q water and loaded into a 10 mL syringe. In parallel, 4 mg of EVs^{A549}-derived membranes in 8 mL of chloroform were loaded into a separate 10 mL syringe, maintaining the 1:2 (*w/w*) FSNs-APTES:EVs^{A549} ratio. The two solutions were simultaneously injected into the micromixer at flow rates of 12 and 24 mL/min, respectively. To ensure sample uniformity, the initial output was discarded for a period corresponding to several residence times (approximately 5 s) until steady-state conditions were fully established. Following immediate phase separation at the outlet, the upper aqueous phase was recovered, containing the microfluidics-assisted membrane-coated FSNs (FSNs-$EVs^{A549}{}_{micro}$).

In this study, we employed a modified 1/16 in. PEEK T-junction (UPCHURCH, USA) integrating at the outlet region a micromachined porous stainless-steel fitting with an average pore size of ∼10 μm. This element facilitates uniform dispersion of the incoming phase into multiple microchannels prior to contact, thereby significantly enhancing interfacial shear and promoting the robust self-assembly of the target nanostructures.

The shear stress generated at the interface between the two immiscible streams provides sufficient energy to trigger the assembly process without requiring external mechanical or ultrasonic input. The porous element acts as a passive mixer, promoting a significant increase in fluid lamellae, thus increasing the surface-to-volume ratio and drastically reducing diffusion path lengths to enable fast and homogeneous mixing at the microscale. Furthermore, the complex geometry of the pores induces chaotic advection, which accelerates mass transfer and ensures a more efficient membrane−nanoparticle interaction compared to conventional bulk mixing.

This design thus outperforms conventional T-junctions by creating a highly defined and distributed contact interface, which is crucial for enhanced surface interaction and the controlled assembly of structures from immiscible phases.[46] Microscale mixing maximizes the interfacial surface area while minimizing diffusion distances, significantly enhancing mass transfer between the organic and the aqueous phase. This facilitates a two-stage assembly process driven by distinct physicochemical interactions. Initially, electrostatic attraction between the negatively charged phospholipid heads and the positively charged FSNs-APTES orients phospholipids toward the silica core, recruiting both intact membrane blocks and individual phospholipids. Subsequently, hydrophobic interactions between exposed hydrophobic lipid tails drive the recruitment of additional unbound phospholipids, completing the bilayer around the NP core.

Both FSNs-$EVs^{A549}{}_{batch}$ and FSNs-$EVs^{A549}{}_{micro}$ were thoroughly characterized by Flow Cytometry to analyze EVs biomarkers, NTA, ζ-potential, and TEM as previously mentioned for the natural EVs^{A549}. TEM analysis provided details to differentiate the thickness of the organic EVs^{A549}-derived membrane assembled on the surface of the NPs. The Fourier Transform Infra-Red (FTIR) spectra of the FSNs-$EVs^{A549}{}_{batch}$ were recorded as previously mentioned. Moreover, the colocalization of the FSNs with FSNs-EVs^{A549} was determined with super-resolution confocal microscopy (ZEISS Elyra 7-Lattice SIM^2). With this aim, FSNs were directly visualized thanks to their intrinsic

https://doi.org/10.1021/acsanm.5c05265
ACS Appl. Nano Mater. XXXX, XXX, XXX−XXX

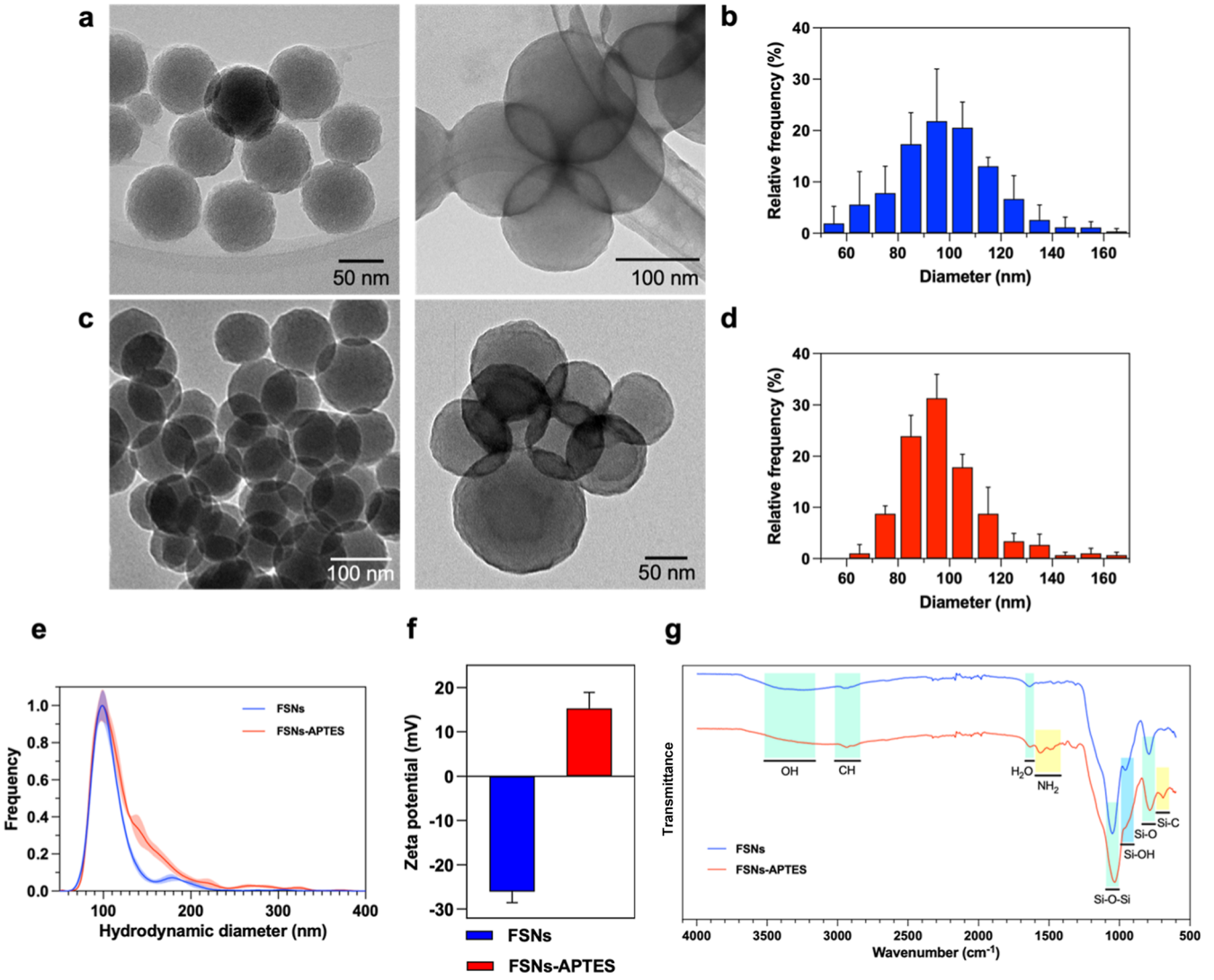

Figure 2. Characterization of FSNs and FSNs-APTES. (a) Representative TEM images of FSNs; (b) FSNs particle size distribution obtained from TEM images (n = 3, 100 events measured in each replicate); (c) TEM images of FSNs-APTES stained with phosphotungstic acid 3%; (d) FSNs-APTES particle size distribution obtained from TEM images (n = 3, 100 NPs measured in each replicate); (e) hydrodynamic diameters of FSNs and FSNs-APTES obtained by NTA (n = 5); (f) ζ-potential measurements (pH 7) of naked and functionalized NPs (n = 5); (g) FTIR spectra of FSNs and FSNs-APTES: common peaks are highlighted in green, FSNs peaks in blue, and FSNs-APTES peaks in yellow.

FITC fluorescence (λ_{ex} = 495 nm), where the EVs^{A549}-derived membranes were fluorescently labeled with PKH67 dye (λ_{ex} = 551 nm) following manufacturer instructions as previously reported.[6]

Internalization and Selectivity Assessment

The cellular uptake and the targeting selectivity of FSNs-EVs$^{A549}{}_{batch}$ and FSNs-EVs$^{A549}{}_{micro}$ were evaluated by confocal microscopy and by flow cytometry. For confocal microscopy characterization, A549, HeLa, and fibroblasts were seeded at a density of 5×10^4 (and 3×10^4 for fibroblasts) on 10 mm coverslips (in a 24-well plate) and allowed to grow for 1 day. Then, FSNs, FSNs-EVs$^{A549}{}_{batch}$, and FSNs-EVs$^{A549}{}_{micro}$ were added at the same concentration (0.03 mg/mL) and incubated for 4 or 24 h. Finally, cells were washed three times with PBS to discard the noninternalized vectors and they were fixed with paraformaldehyde 4% and stained with phalloidin to label the cytoplasmic actin (λ_{ex} = 561 nm). FSNs-based agglomerates of the vectors were observed inside the cells thanks to the FITC fluorescence (λ_{ex} = 488 nm) of the NPs and nuclei were stained with ProLong Glass Antifade Mountant with NuncBlue (λ_{ex} = 405 nm). Cells were observed using a Zeiss LSM 880 spectral-confocal microscope Zeiss LSM 880. Pixel intensity inside cells cytoplasm incubated with the different vectors was semiquantified from the Z-stack images to compare their uptake in the target and off-target cells.

The cells' capability to internalize FSNs, FSNs-EVs$^{A549}{}_{batch}$, and FSNs-EVs$^{A549}{}_{micro}$ was also evaluated by flow cytometry. Briefly, 2×10^5 A549, 2×10^5 HeLa cells, or 1.2×10^5 fibroblasts were seeded onto a 6-well plate and after 24 h, they were incubated with the different vectors (0.03 mg/mL) for 4 h. After this time-point, cells were collected in PBS and analyzed by flow cytometry using a Gallios Flow Cytometer (Beckman Coulter). The median fluorescence intensity was considered to assess the NPs internalization. For detection, an excitation wavelength of 488 nm was used. Samples were analyzed acquiring at least 10,000 events.

Statistical Analysis

The biological experiments were performed at least in triplicate. All the data are indicated as mean ± SD. Statistical analysis of the significant differences among the means was carried out by one-way or two-way analysis of variance (ANOVA) for multiple comparisons by Dunnett's multiple comparisons test (GraphPad Prism Software). Statistically significant differences were expressed as follows: $*p < 0.05$; $**p < 0.01$; $***p < 0.001$ y $****p < 0.0001$.

https://doi.org/10.1021/acsanm.5c05265
ACS Appl. Nano Mater. XXXX, XXX, XXX−XXX

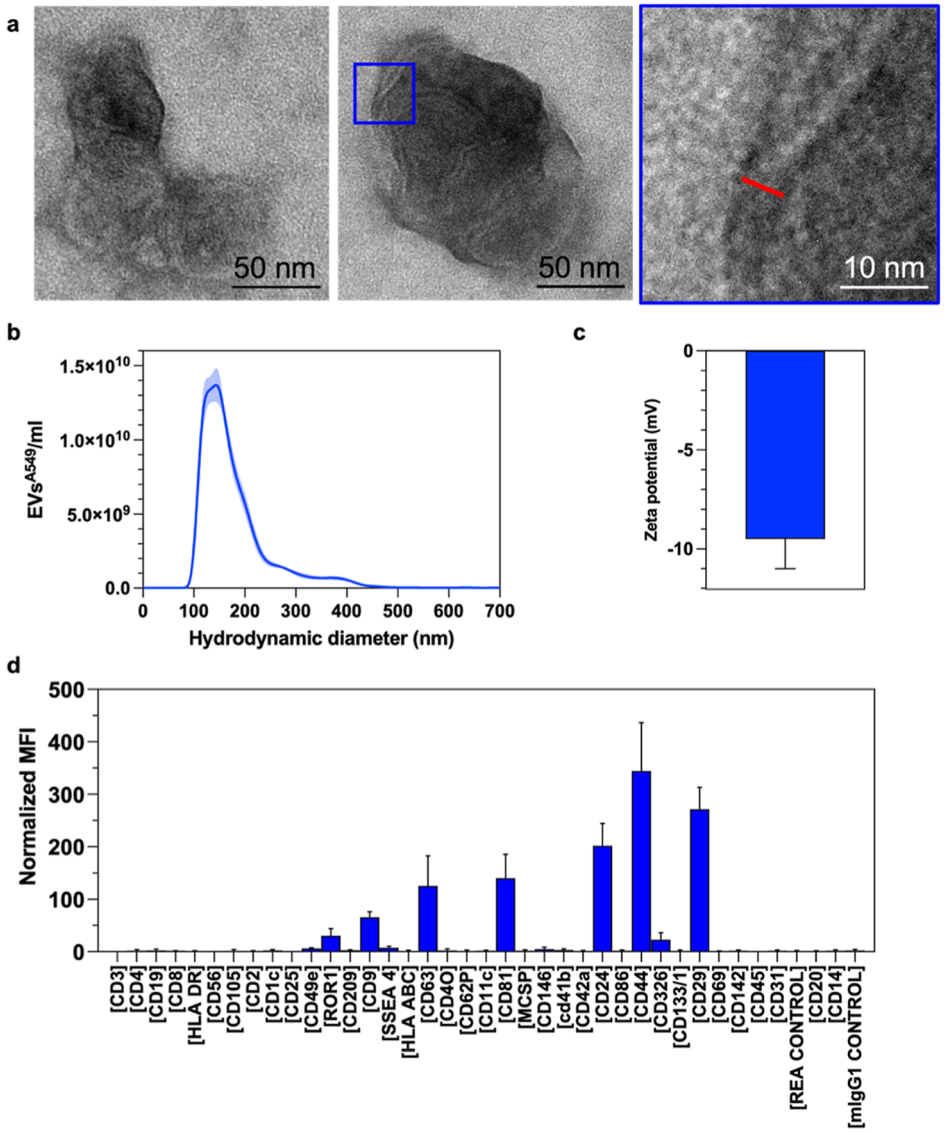

Figure 3. Characterization of EVs^{A549}. (a) Representative TEM images of EVs isolated from A549 cells culture supernatant. Zoom on the right side highlights the thickness of their lipid membrane, which is clearly visible; (b) size distribution of EVs^{A549} obtained by NTA (n = 5); (c) ζ-potential (pH 7) of these EVs (n = 5); (d) EVs-associated markers analyzed by flow cytometry (n = 3).

RESULTS AND DISCUSSION

FSNs Characterization

TEM analysis confirmed the formation of monodisperse and homogeneous FSNs with a spherical structure (Figure 2a) and mean diameters of 98.5 ± 16.9 nm (Figure 2b). The hydrodynamic diameter of the FSNs was obtained by NTA, revealing the monodisperse NPs population centered at about 113.7 ± 36.4 nm with a good colloidal stability, corresponding well to TEM analysis (Figure 2d). The ζ-potential of the FSNs was −26.1 ± 2.5 mV (Figure 2f) in agreement with the presence of Si−OH groups in the surface of the NPs, which at neutral pH are negatively charged (Si−O$^-$). FSNs were positively functionalized using APTES prior to the assembly of EVs^{A459}-derived membranes. The positively charged amino-propyl groups on the surface of the FSNs-APTES are expected to promote their coupling with EVs membranes by electrostatic interactions (primary amines are protonated at neutral pH and the EVs are negatively charged).[47]

Figure 2c also shows TEM images of positively charged FSNs (FSNs-APTES) stained with phosphotungstic acid (PTA) 3%, with their size distribution (Figure 2d) and hydrodynamic size (Figure 2e). The morphology, shape, and size of the NPS were not significantly altered after their functionalization. The distribution of FSNs-APTES obtained from TEM images displayed an average diameter of 99.0 ± 21.7 nm, while NTA analysis gave a mean hydrodynamic diameter of 127.8 ± 36.4 nm, slightly superior to that of the naked FSNs possibly reflecting the decrease of the repulsive electrostatic force between NPs, as shown next. The surface charge inversion from −26.1 ± 2.46 mV to 15.3 ± 3.6 mV for FSNs-APTES (Figure 2f) corroborated the successful functionalization with amino groups. The functionalization of the FSNs surface was also confirmed by FTIR spectroscopy (Figure 2g). Both spectra show the characteristic fingerprint bands of the silica structures Si−O−Si (1050 cm^{-1}) and Si−O (950 cm^{-1}), together with C−H (2950 cm^{-1}) from the FITC-APTES dye conjugate. Nonfunctionalized FSNs show a more prominent Si−OH peak (800 cm^{-1}) attributed to free silanol

https://doi.org/10.1021/acsanm.5c05265
ACS Appl. Nano Mater. XXXX, XXX, XXX−XXX

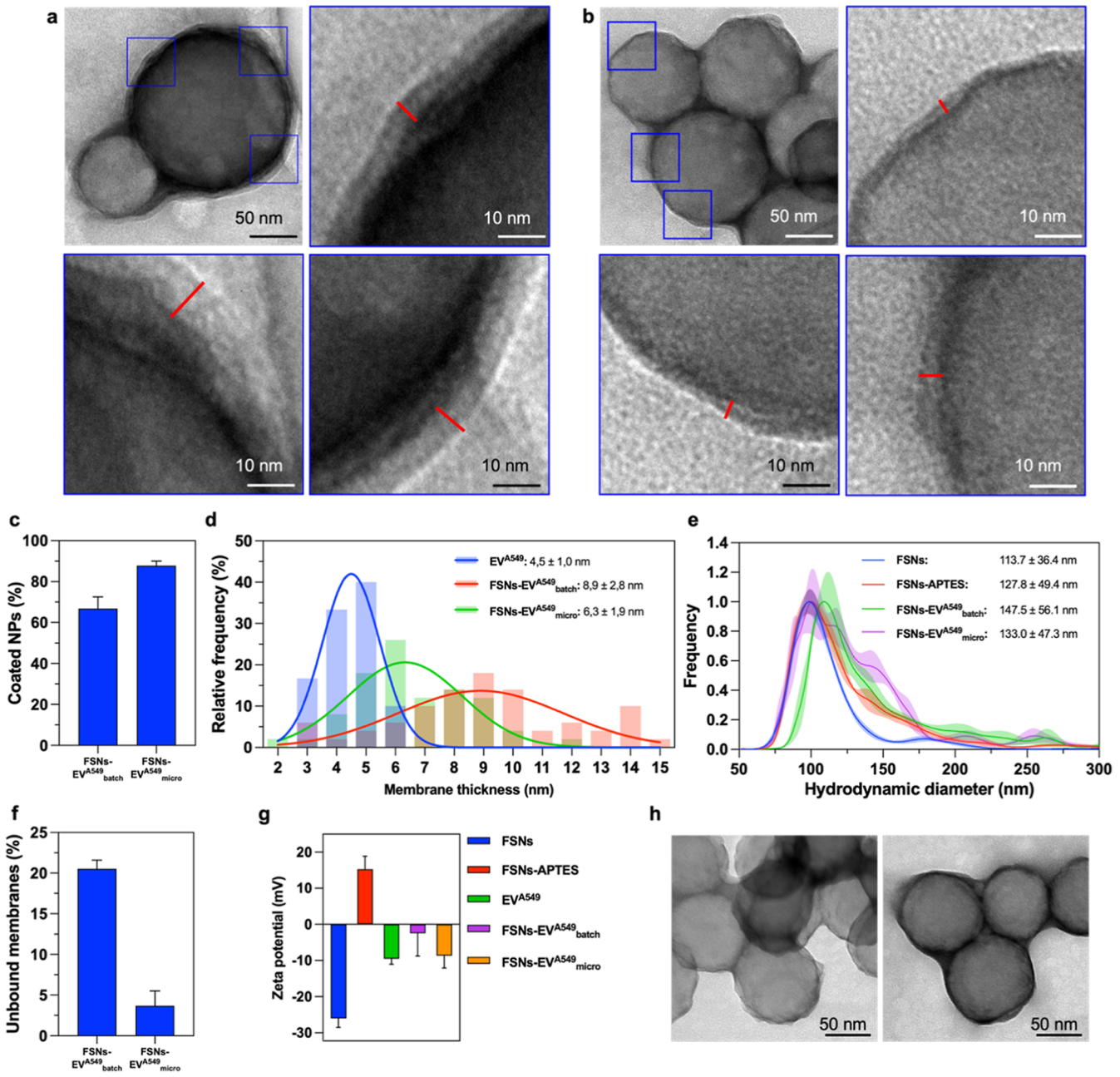

Figure 4. Characterization of FSNs-EVs$^{A549}_{batch}$ and FSNs-EVs$^{A549}_{micro}$. (a) Representative TEM images of FSNs-EVs$^{A549}_{batch}$. (b) Representative TEM images of FSNs-EVs$^{A549}_{micro}$. The zoom in (a,b) clearly shows the presence of the organic shell from the membranes assembled around the NPs core visible thanks to a negative staining to contrast this organic shell; (c) coating efficiency of the FSNs with both explored techniques (n = 3, 50 events evaluated in each replicate); (d) thickness of the EVs-derived membrane shell around the NPs for both preparation techniques and comparison with the natural EVs^{A549} membrane thickness (n = 90); (e) size distribution obtained by NTA of the formulated FSNs-EVs$^{A549}_{batch}$ and FSNs-EVs$^{A549}_{micro}$ and comparison with naked and positive-functionalized NPs (n = 5); (f) percentage of unbound membranes after batch and microfluidic coating of FSNs-APTES (n = 3); (g) ζ-potential (pH 7) evolution of the different NPs formulations (n = 5); (h) TEM images of SNs-EVs$^{A549}_{micro}$. The EV-associated membrane can be clearly observed around the NPs.

(Si−OH) surface groups. The band intensity is reduced for FSNs-APTES, while bands for amino groups of APTES anchored on the surface of the NPs (1525 cm^{-1}) and Si−C APTES bonds (700 cm^{-1}) are detected.

Assembling of FSNs-EVs$^{A549}_{batch}$ and FSNs-EVs$^{A549}_{micro}$: Batch versus Microfluidics

Previous works dealing with membrane-coated NP hybrids typically assembled these structures following three steps: (1) isolation of the membrane from cells (or in this work from EVs), (2) drying and separation of the membranes, and (3) assembling the membranes onto/around the NPs using direct contact approaches, extrusion filters, or ultrasonic treatment methods.[48−51]

Before isolating EVs^{A549} membranes and assembling them on the surface of FITC-APTES, natural EVs^{A549} were thoroughly characterized in this work by physicochemical and biological techniques. The TEM images of EVs^{A549} isolated from culture supernatants by serial ultracentrifugation cycles are included in Figure 3a. A spherical shape and the

https://doi.org/10.1021/acsanm.5c05265
ACS Appl. Nano Mater. XXXX, XXX, XXX−XXX

characteristic phospholipidic membrane could be observed in many images (for instance, see enlarged areas of TEM images in Figure 3a). This bilayer exhibits a measured thickness of 4.5 ± 1.0 nm (in concordance with 5 nm thickness reported).[52] According to NTA measurements (Figure 3b), the mean particle diameter was 178.7 ± 73.4 nm in line with previous data reported for these cancer EVs.[45] The measured surface charge of EVs^{A549} was −9.5 ± 1.5 mV (Figure 3c), attributed to the negatively charged phospholipids and proteins present on the EVs membrane at pH 7.[8]

Flow cytometry was used for the evaluation of the EVs-associated surface markers (Figure 3d). EVs^{A549} were enriched in tetraspanins such as CD81, CD9, and CD63 (often referred as common EV surface markers)[53] that were strongly positive, while CD24, CD44, and CD29 also exhibited strong signals. These proteins have also been reported as main markers detected in EVs.[54]

EVs-derived membranes are mainly composed by phospholipids that orientate their polar heads toward the external environment in aqueous media. These polar heads contain phosphate groups that are negatively charged.[55] Moreover, the phospholipids functional groups (i.e., phosphatidylserine or phosphatidylinositol of the EVs membranes) confer the whole membrane an overall negative surface charge. In contrast, FSNs-APTES are protonated at neutral pH,[56] acquiring a positive surface charge. This difference in ζ-potential between NPs and EVs-associated membranes guides the assembly of the membranes around the NPs core due the attractive electrostatic forces (as in the natural EVs). Entropic forces also favor this process since the phospholipids tend to reorganize themselves into stable bilayers, so that they orient their polar heads toward the surface of the NPs and toward the aqueous exterior medium, hiding their hydrophobic fraction in the interior of the bilayer. This arrangement minimizes the free energy of the system, generating a thermodynamically favorable conformation.[57,58] This behavior, together with the attraction of the surface charges, favors their self-assembly around the FSNs-APTES.

In this work, we selected EV membranes from A549 cells due to their expected tropism toward these cancer cells.[45] After FSNs synthesis and functionalization, EVs^{A549}-derived membranes were isolated following Folch's method[17] with slight modifications, as described in the experimental part. These membranes were then assembled onto the surface of FSNs-APTES following two different strategies, depicted in Figure 1. A batch strategy was explored in the first place. In this case, EVs membranes were dried on the surface of a glass vial, and $FSNs\text{-}EVs^{A549}{}_{batch}$ were prepared by thin film hydration. Briefly, the obtained dried EVs^{A549}-derived membrane films were hydrated by directly putting the dried films into contact with an aqueous solution containing the FSNs-APTES NPs to allow their adsorption on the surface of the particles. Finally, the mixture was sonicated for 10 min (Figure 1). On the other hand, the coating of the nanoparticles was also performed using a micromixer to assemble EV membranes onto FSNs-APTES by mixing two immiscible streams, as stated in the experimental part. In this way, $FSNs\text{-}EVs^{A549}{}_{micro}$ were obtained.

The presence of the membrane shell around the surface of the NPs was evaluated by TEM. Figure 4a,b shows TEM images of $FSNs\text{-}EVs^{A549}{}_{batch}$ and $FSNs\text{-}EVs^{A549}{}_{micro}$, respectively. An organic shell that surrounds the NPs was consistently observed for both samples corresponding to the coating of the FSNs-APTES nanoparticles by the EVs membranes. Moreover, TEM images allowed us to analyze the coating efficiency (Figure 4c) as well as the thickness of the EV membrane around the NPs (Figure 4d) by looking at a sufficient number of NPs ($N > 90$) to have robust statistics. The results indicate that the microfluidic strategy is clearly more efficient at NP coating. Thus, if we define a coated NP as a NP with any amount of visible membrane on its surface, a considerably higher percentage of coated NPs was obtained by the microfluidic approach compared with the discontinuous process (87.8% and 66.8%, respectively), with the rest being naked NPs. This can be attributed to the more efficient mixing achieved in the passive micromixer, where interfacial shear stress between immiscible streams facilitates the contact between the membranes and the NPs, reducing the probability of naked NPs.

Coating efficiency was also assessed by weighing the remaining unbound membranes after both coating procedures on a microbalance. Figure 4f shows how the microfluidic-assisted coating transfers most of the lipid membranes (only 3.7% remaining), achieving a better coating of the EVs compared to the batch method (20.5% unbound membranes).

TEM observations further validate these findings by enabling the evaluation of membrane thickness (Figure 4d) at a single-particle level across multiple surface points rather than relying on population averages. For the $FSNs\text{-}EVs^{A549}{}_{micro}$, the membrane thickness fitted a Gaussian distribution with a mean value (6.3 ± 1.9 nm) closely approximating the ∼5 nm thickness characteristic of natural EV bilayers. In contrast, the $FSNs\text{-}EVs^{A549}{}_{batch}$ membranes exhibited a non-Gaussian distribution; their mean thickness (8.9 ± 2.8 nm) more closely resembled a double-membrane coating. Furthermore, a prominent secondary peak at 14 nm in the batch samples indicates the formation of uncontrolled multibilayered structures across a significant fraction of the NP population. These results further illustrate how the batch process does not allow for fine control, resulting in the formation of a more heterogeneous $FSNs\text{-}EVs^{A549}{}_{batch}$ population with different coating thicknesses that deviate more from the natural structure of the EVs coating.

While both methods involve membrane processing, the batch method's reliance on a fully dried lipid film often results in the visible aggregation of the phospholipids. These macroscopic aggregates are difficult to disperse uniformly, even with ultrasonication. Our microfluidic protocol avoids this dehydration-induced aggregation by maintaining the EV membranes in a liquid phase. This allows for a more controlled matter transfer and a significantly more homogeneous coating compared to the batch methodology.

The NTA measurements displayed in Figure 4e evidence FSNs surface modifications, which consequently increase the NPs' effective diameter by addition of new surface layers. NTA analysis showed a particle size distribution that correlates well with the TEM images just discussed (113.7 ± 36.4, 127.8 ± 49.4, 147.5 ± 56.1, and 133.0 ± 47.3 nm for FSNs, FSNs-APTES, $FSNs\text{-}EVs^{A549}{}_{batch}$, and $FSNs\text{-}EVs^{A549}{}_{micro}$, respectively). There is a progressive shift in the average particle size from FSNs to FSNs-APTES and then to $FSNs\text{-}EVs^{A549}$, reflecting the successful outcomes of functionalization and membrane assembling steps on the surface of the NPs, with a somewhat larger size for $FSNs\text{-}EVs^{A549}{}_{batch}$, as expected from the above discussion. Figure 4g includes the evolution of the ζ-potential. Surface charge changes evidenced the partial or total

https://doi.org/10.1021/acsanm.5c05265
ACS Appl. Nano Mater. XXXX, XXX, XXX−XXX

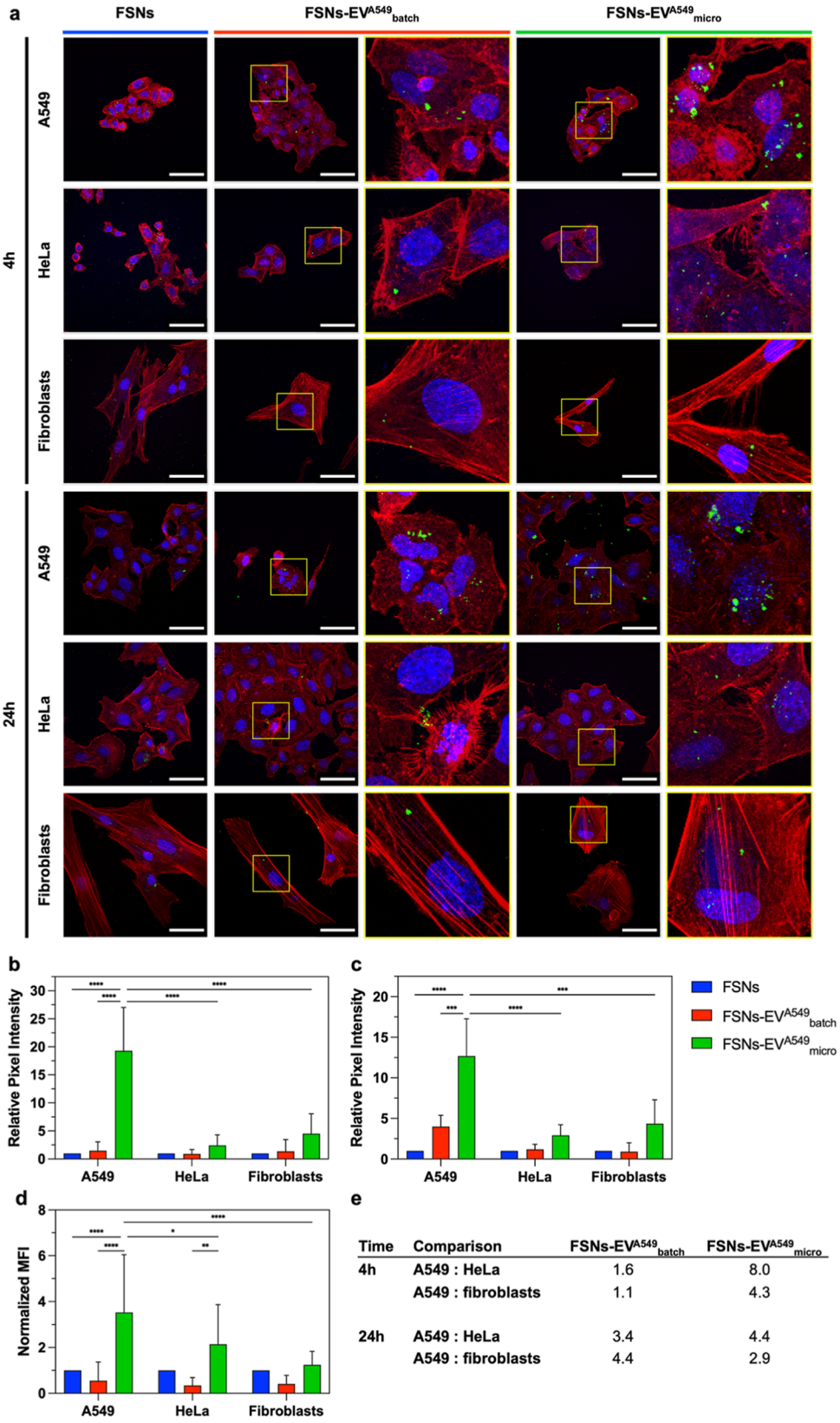

Figure 5. Evaluation of internalization of FSNs-EVs$^{A549}_{batch}$ and FSNs-EVs$^{A549}_{micro}$ in target cells (A549) and off-target cells (HeLa and fibroblasts). (a) Confocal images of the three cell lines after incubation during 4 and 24 h with FSNs, FSNs-EVs$^{A549}_{batch}$, and FSNs-EVs$^{A549}_{micro}$ (0.05 mg/mL of NPs). The insets show FITC-labeled NPs internalized in cells; confocal semiquantification of FITC fluorescence inside the cells relative to FSNs at the (b) 4 h and (c) 24 h time points (n = 3); (d) flow cytometry-based uptake yields in the three cell lines expressed in median fluorescence intensity relative to FSNs (n = 9); (e) quantitative assessment of the selectivity ratios of FSNs-EV$^{A549}_{batch}$ and FSNs-EV$^{A549}_{micro}$ between parental A549 cells and off-target cells at each time point. Scale bar for confocal images: 50 μm.

https://doi.org/10.1021/acsanm.5c05265
ACS Appl. Nano Mater. XXXX, XXX, XXX−XXX

coating of the positively charged FSNs-APTES (15.3 ± 3.6 mV) with the EVs^{A549}-derived membranes, giving postcoating values of −2.4 ± 6.32 and −8.7 ± 3.4 mV for the batch and the microfluidic approaches, respectively. The less electronegative ζ-potential of FSNs-EVs$^{A549}{}_{batch}$ suggests a more heterogeneous coating of these NPs, with part of the core FSNs-APTES surface still remaining uncoated and thus contributing to a more positively charged NP. Moreover, zeta potential measurements of FSNs-EVs$^{A549}{}_{batch}$ exhibited greater variability across different syntheses compared to FSNs-EVs$^{A549}{}_{micro}$, as indicated by the larger error bars in Figure 4g, demonstrating the benefits of this new microfluidic approach. Additional images of coated SNs-EVs$^{A549}{}_{micro}$ in Figure 4h confirm the homogeneity of the microfluidic approach.

FTIR analysis of EVs^{A549}, FSNs, FSNs-EVs$^{A549}{}_{batch}$, and FSNs-EVs$^{A549}{}_{micro}$ confirmed the association of the phospholipid coating and the silica core (Figure S2) together with the bands corresponding to silica (previously described in Figure 2g); the characteristic phospholipid fingerprint region was identified.[59−61] Fatty acid chains contain numerous methyl groups that present a singular signature on both isolated membranes and FSNs-EV hybrids. A cluster of peaks can be found at 2960, 2920, 2870, and 2850 cm^{-1} belonging to methyl and methylene asymmetric stretching ($\nu_{as}{}^{CH3}$ and $\nu_{as}{}^{CH2}$) and methyl and methylene symmetric stretching ($\nu_{as}{}^{CH3}$ and $\nu_{as}{}^{CH2}$), respectively. A second set of two smaller peaks was found at 1450 and 1380 cm^{-1} that were attributed to methyl asymmetric and symmetric bending ($\gamma_{as}{}^{CH3}$ and $\gamma_{s}{}^{CH3}$). Similarly, the carbonyl groups also present a stretching peak at 1735 cm^{-1} ($\nu^{C=O}$). Lastly, the bands of the phosphate groups were observed between 1000 and 1300 cm^{-1}, highlighting the symmetric and asymmetric stretching bands of phosphodiester bonds ($\nu_{s}{}^{PO2}$ and $\nu_{as}{}^{PO2}$), that link the functional groups of the phospholipids;[62] at 1080 and 1250 cm^{-1}, these peaks are buried under the silica peaks of the FSNs.

The expression of the characteristic EVs-associated membrane markers assembled on the surface of the NPs was assessed by flow cytometry. To minimize interferences from the fluorescence signal of the FSNs, FITC-free silica NPs (SNs) were employed. Figure S3 compares the EVs-associated marker expression pattern of SNs coated with EVs^{A549}-derived membranes following the batch and the microfluidic strategies, SNs-EVs$^{A549}{}_{batch}$ and SNs-EVs$^{A549}{}_{micro}$, respectively. It can be seen that in both cases, the three characteristic markers are present, with relative intensities among themselves that follow the pattern (CD9 < CD63 < CD81) found for the pristine EVs membranes (Figure 3d), although with a higher overall intensity for the microfluidic-coated NPs.

Finally, to further evaluate the efficacy of the self-assembly of EVs^{A549} membranes around the FSNs, fluorescence colocalization analysis was performed. FSNs were visualized thanks to the FITC fluorescence. EVs^{A549}-derived membranes were labeled with PKH26, a lipophilic dye, exhibiting red emission. Although the resolution limit dictated by Abbey's law does not permit appreciation of the core−shell structure, the observation of the spots collected from the two channels suggests the colocalization of EVs-associated membranes and NPs. Yellow spots (green emission from the NPs superimposed on the red emission of membranes) were observed in the panel of Figure S4. This means that the visible objects in both channels were colocalizing as expected, given the coating of the membranes around the particles.

Before evaluating the internalization and the selectivity of FSNs-EVs$^{A549}{}_{batch}$ and FSNs-EVs$^{A549}{}_{micro}$ in different cell lines, the biocompatibility of FSNs and FSNs-APTES in A549 cells was studied (Figure S5) to assess the doses that could be used in the incubation. The Blue cell viability assay showed that both naked and APTES-functionalized NPs did not significantly decrease cell viability at the studied doses (from 1 to 0.01 mg/mL) at any of the tested time-points (24, 48, and 72 h). This was expected, as Si NPs are nontoxic and highly biocompatible.[63−65] The dose of 0.03 mg/mL FSNs was chosen for the subsequent experiments to evaluate whether the EVs-membrane coating provides the NPs with targeting properties against their parental cells.

Uptake and Selectivity Experiments

NPs uptake is strongly influenced by physical features (morphology, size, and shape) and surface chemistry.[66,67] However, cell membrane-coated NPs are being investigated in biomimetic nanoengineering approaches[68] as they are expected to provide important advantages such as increased targeting selectivity and immune system evasion. As an alternative, it is also possible to coat the NPs using membranes from EVs rather than whole membranes from cells.[16,69,70] Although several difficulties must be overcome (such as the complexity of the process and the requirement of precise techniques to harvest EVs membranes), these NPs coated with EVs membranes would in principle better mimic the characteristics of natural EVs and this is the reason why they were chosen in this work.

To evaluate the role of EVs^{A549}-derived membranes in the tumor-targeting efficiency of FSNs, confocal microscopy and flow cytometry techniques were employed. The preferential tropism of both FSNs-EVs$^{A549}{}_{batch}$ and FSNs-EVs$^{A549}{}_{micro}$ was tested in three cell lines: the parental EVs-producer cell line A549, HeLa cells as another example of tumoral cells, and fibroblasts, as an example of control healthy cells. Each of these cell culture media was supplemented with 0.03 mg/mL of one of these NPs: FSNs, FSNs-EVs$^{A549}{}_{batch}$, and FSNs-EVs$^{A549}{}_{micro}$, keeping constant the amount of NPs in the four formulations to make the uptake kinetics comparable. Then, the NPs internalization was evaluated after 4 and 24 h. Figure 5a includes confocal microscopy images visualizing the uptake of the distinct FSNs hybrids, in green, with actin filaments and nuclei stained in red and blue, respectively. To evaluate the uptake efficiency, the intracellular FITC fluorescence was quantified and normalized to the total cell area. The resulting ratios of mean fluorescence intensity, comparing each FSN-EV hybrid to naked FSNs, are presented in Figure 5b,c.

These results clearly show that when FSNs were engineered with EVs^{A549} membranes, their uptake increased compared to naked nanoparticles. Of note, the coating prepared using microfluidic technology (FSNs-EVs$^{A549}{}_{micro}$) is clearly more efficient to foster internalization and preserves EV-targeting properties compared to thin film hydration samples (FSNs-EVs$^{A549}{}_{batch}$) at short (4 h) and long (24 h) incubation times. Thus, regarding internalization in A549 cells at the 4 h time point (Figure 5b), it can be observed that while coating NPs with A549 EVs membranes using the batch procedure increased uptake by 50% (1.5-fold compared to naked FSNs), for the FSNs-EVs$^{A549}{}_{micro}$, the uptake was much higher (19.3-fold). This tendency is still observed at longer incubation times (24 h) with 4.0- and 12.7-fold increases for the batch and microfluidic hybrids, respectively.

https://doi.org/10.1021/acsanm.5c05265
ACS Appl. Nano Mater. XXXX, XXX, XXX−XXX

Comparing the internalization of these same vehicles in different cell lines, the preferential uptake by parental A549 cells is also clear. After a 4 h incubation with FSNs-EVs$^{A549}_{micro}$, A549 cells show a 19.3-fold increase in fluorescence compared to only 2.4- and 4.5-fold increases when incubated with HeLa cells and fibroblasts, respectively (Figure 5b). Again, this is as well-observed at the 24 h time point (Figure 5c), with fold-increases of 12.7, 2.9, and 4.4 for A549 cells, HeLa cells, and fibroblasts, respectively, in agreement with the preferential targeting reported for EVs.[8]

Although FSNs-EVs$^{A549}_{batch}$ were also preferentially internalized in A549 cells compared to the other cell lines (HeLa and fibroblasts), the figures were much lower (1.5-, 0.9-, and 1.4-fold at 4 h and 4.0, 1.2, and 0.9 at 24 h, respectively). These comparisons are clearer in Figure 5e, where the selectivity ratios between target parental and off-target cells for the different hybrids and times are stated. Microfluidic-engineered hybrids exhibited a significantly higher selectivity toward A549 cells compared to that toward off-target cells, with targeting ratios ranging from 2.9 to 8.0. In contrast, the batch-hybrid counterparts showed markedly lower performance, with selectivity ratios only reaching between 1.1 and 4.0. These results indicate that the coating achieved by the microfluidic method not only is more homogeneous as shown above but also preserves better the arrangement of the proteins and other fingerprint molecules in the membrane, facilitating the uptake on their own producer cells.

The internalization of the different NPs across the three cell lines was quantified via flow cytometry, analyzing the Median Fluorescence Intensity (MFI) to assess uptake at a single-cell level across a large population (>10,000 events). To isolate the influence of the EV membrane on cellular tropism, MFI values were corrected for cell-specific autofluorescence and expressed as a selectivity ratio between the hybrids and the bare FSNs. This normalization accounts for the baseline endocytic activity of each cell line, ensuring that any observed increase in fluorescence is directly attributable to the EV-membrane-mediated recognition. Consequently, higher MFI ratios in the A549 cell line serve as a quantitative indicator of the targeting capabilities of the engineered hybrids. As shown in Figure 5c, the internalization data after 4 h exhibited a very similar pattern compared to confocal microscopy images reflecting again the preferential targeting by FSNs-EVs$^{A549}_{micro}$ toward A549 target cells. Indeed, A549 cells showed a substantial 3.5-fold increase in fluorescence intensity when incubated with FSNs-EVs$^{A549}_{micro}$ compared with the naked FSNs. This effect was not as prominent in HeLa cells or fibroblasts, which only showed a nonsignificant 2.1 and 1.2 increase, respectively (significantly lower compared to the 3.5 factor in parental A549 cells). The increase on MFI compared to FSNs reveals that all cell types are able to internalize more FSNs-EVs$^{A549}_{micro}$, even nonparental cells due to nonspecific membrane interactions, but the distinct molecular signature on the coating of FSNs-EVs$^{A549}_{micro}$ allows for even greater uptake in its parental A549 cell line.

For the FSNs-EVs$^{A549}_{batch}$, a similar trend was observed. In these, the relative MFI was 0.5, 0.3, and 0.4 for A549, HeLa cells, and fibroblasts, respectively. Thus, although when FSNs were coated with the A549 membranes, they showed a slight preference (nonsignificant) toward their membrane-producers' cells, their internalization yields were significantly lower compared to the microfluidic-fabricated hybrids. This was attributed to the high heterogeneity on the membrane assembly when the batch process was followed, leading to a low ζ-potential and increased aggregation of FSNs-EVs$^{A549}_{batch}$ (see Figure 4b). We hypothesize that FSNs-EVs$^{A549}_{batch}$ form greater NP aggregates, which hinder their uptake by the different cell types. On the other hand, the coating of FSNs-EVs$^{A549}_{micro}$ is much more homogeneous ensuring a better distribution and individuality of each NP and allows for better membrane-mediated interactions between the NP-EV hybrids and the target cells. These findings were the result of 9 biological replicates using 4 independent FSNs syntheses and EV^{A549} coatings. Figure S6 shows no significant differences between replicates, highlighting the advantage of the microfluidic-assisted coating approach also in terms of batch-to-batch reproducibility. Although not statistically significant, the internalization of FSNs-EVs$^{A549}_{batch}$ exhibited slightly higher uptake rates in the second set of replicates, indicating a less controlled process compared to the consistent performance of the FSNs-EVs$^{A549}_{micro}$ samples.

CONCLUSIONS

Artificial vectors that attempt to replicate the properties of natural EVs have been built using NPs composed of a fluorescent silica core surrounded by EVs-based membranes. The fabrication uses a self-assembly process, leveraging the positive charge of APTES-functionalized silica to achieve coating by negatively charged EVs membrane fragments. However, the way to put into contact the core nanoparticles and the coating membranes has a strong influence on the final properties of the resulting hybrids. In particular, the microfluidic strategy, based on shear-stress-driven mixing in a passive micromixer, allowed a fine control over the membrane assembly process and preserved better the complex membrane structure (EVs markers, phospholipids, thickness, and size). This approach minimized heterogeneities and ensured consistent coating thickness, overcoming limitations typically observed in batch preparations. As a consequence, these FSNs-EVs$^{A549}_{micro}$ exhibited higher internalization yields (3.5-fold) and targeting properties against A549 cells compared to nonfunctionalized FSNs. Altogether, these results evidenced how this innovative microfluidic approach in the coating of NPs with EVs-derived membranes is a useful technique to create EV-mimicking hybrids that preserve better the targeting molecules and capabilities of natural EVs.

ASSOCIATED CONTENT

Supporting Information

The Supporting Information is available free of charge at https://pubs.acs.org/doi/10.1021/acsanm.5c05265.

Scheme containing reactions for FSNs synthesis and functionalization; FTIR analysis of FSNs-EVs$^{A549}_{batch}$, FSNs-EVs$^{A549}_{micro}$, and EVs^{A549}; expression of the characteristic EVs-associated membrane markers assembled on the surface of the NPs by Flow Cytometry; super-resolution images obtained on an Elyra 7 (ZEISS) microscope; and biocompatibility test of FSNs and FSNs-APTES on A549 cells and reproducibility of flow cytometry-based uptake yields in the three cell lines (PDF)

https://doi.org/10.1021/acsanm.5c05265
ACS Appl. Nano Mater. XXXX, XXX, XXX−XXX

AUTHOR INFORMATION

Corresponding Authors

Víctor Sebastián − *Instituto de Nanociencia y Materiales de Aragón (INMA), CSIC-Universidad de Zaragoza, Zaragoza 50018, Spain; Department of Chemical and Environmental Engineering, Institute of Nanoscience and Materials of Aragon, Universidad de Zaragoza, Zaragoza 50009, Spain; Instituto de Investigación Sanitaria de Aragón (IIS Aragón), Zaragoza 50009, Spain; Networking Research Center in Biomaterials, Bioengineering and Nanomedicine (CIBER-BBN), Instituto de Salud Carlos III, Madrid 28029, Spain; Laboratorio de Microscopías Avanzadas, Univ. de Zaragoza, Zaragoza 50018, Spain;* orcid.org/0000-0002-6873-5244; Email: victorse@unizar.es

María Sancho-Albero − *Instituto de Nanociencia y Materiales de Aragón (INMA), CSIC-Universidad de Zaragoza, Zaragoza 50018, Spain; Department of Chemical and Environmental Engineering, Institute of Nanoscience and Materials of Aragon, Universidad de Zaragoza, Zaragoza 50009, Spain; Instituto de Investigación Sanitaria de Aragón (IIS Aragón), Zaragoza 50009, Spain; Networking Research Center in Biomaterials, Bioengineering and Nanomedicine (CIBER-BBN), Instituto de Salud Carlos III, Madrid 28029, Spain;* orcid.org/0000-0001-8762-5457; Email: msancho@unizar.es

Authors

Pablo Alonso-Campos − *Instituto de Nanociencia y Materiales de Aragón (INMA), CSIC-Universidad de Zaragoza, Zaragoza 50018, Spain; Department of Chemical and Environmental Engineering, Institute of Nanoscience and Materials of Aragon, Universidad de Zaragoza, Zaragoza 50009, Spain; Instituto de Investigación Sanitaria de Aragón (IIS Aragón), Zaragoza 50009, Spain*

Francisco Balas − *Instituto de Nanociencia y Materiales de Aragón (INMA), CSIC-Universidad de Zaragoza, Zaragoza 50018, Spain; Department of Chemical and Environmental Engineering, Institute of Nanoscience and Materials of Aragon, Universidad de Zaragoza, Zaragoza 50009, Spain; Networking Research Center in Biomaterials, Bioengineering and Nanomedicine (CIBER-BBN), Instituto de Salud Carlos III, Madrid 28029, Spain;* orcid.org/0000-0001-5512-0075

Jose L. Hueso − *Instituto de Nanociencia y Materiales de Aragón (INMA), CSIC-Universidad de Zaragoza, Zaragoza 50018, Spain; Department of Chemical and Environmental Engineering, Institute of Nanoscience and Materials of Aragon, Universidad de Zaragoza, Zaragoza 50009, Spain; Instituto de Investigación Sanitaria de Aragón (IIS Aragón), Zaragoza 50009, Spain; Networking Research Center in Biomaterials, Bioengineering and Nanomedicine (CIBER-BBN), Instituto de Salud Carlos III, Madrid 28029, Spain; Escuela Politécnica Superior, Universidad de Zaragoza, Huesca 22071, Spain;* orcid.org/0000-0002-4546-4111

Jesus Santamaría − *Instituto de Nanociencia y Materiales de Aragón (INMA), CSIC-Universidad de Zaragoza, Zaragoza 50018, Spain; Department of Chemical and Environmental Engineering, Institute of Nanoscience and Materials of Aragon, Universidad de Zaragoza, Zaragoza 50009, Spain; Instituto de Investigación Sanitaria de Aragón (IIS Aragón), Zaragoza 50009, Spain; Networking Research Center in Biomaterials, Bioengineering and Nanomedicine (CIBER-BBN), Instituto de Salud Carlos III, Madrid 28029, Spain;* orcid.org/0000-0002-8701-9745

Complete contact information is available at: https://pubs.acs.org/10.1021/acsanm.5c05265

Author Contributions

The manuscript was written through contributions of all authors. All authors have given approval to the final version of the manuscript.

Funding

The authors thank the Spanish Government, University, Innovation and Science Ministry (CONCERT project). PA-C thanks the Spanish Government for a FPU PhD research fellowship. VS acknowledges funding from project PID2024-160339OB-I00 and PID2021-127847OB-I00 MCIN/AEI/10.13039/501100011033. MS-A thanks the AECC for postdoctoral research fellowship funding (POST-D234966SANC), "Ayuda a Talento AECC 2023," and for a Ramón y Cajal Fellowship (RYC2024-050017-I). The group thanks the Spanish National Research Council (CSIC) (Beca JAE Intro 2024). We thank "Centro de Excelencia Severo Ochoa" (CEX2023-001286 S).

Notes

The authors declare no competing financial interest.

ACKNOWLEDGMENTS

We would like to thank the Scientific Services of the Aragon Institute of Health Sciences (IACS), specifically the Flow Cytometry Service and the Microscopy and Imaging. The synthesis of materials has been performed by the Platform of Production of Biomaterials and Nanoparticles of the NANBIOSIS ICTS, more specifically by the Nanoparticle Synthesis Unit (Unit 9) of the CIBER in BioEngineering, Biomaterials and Nanomedicine (CIBER-BBN). The TEM studies were conducted at the Laboratorio de Microscopias Avanzadas-LMA, Instituto de Nanociencia y Materiales de Aragon, Universidad de Zaragoza, Spain (SAI and ICTS ELECMI).

ABBREVIATIONS

NPs, nanoparticles; EVs, extracellular vesicles; FSNs, fluorescent silica NPs; TEM, Transmission Electron Microscopy; NTA, Nanoparticle Tracking Analysis; EVs^{A549}, A549-derived EVs; $FSNs\text{-}EVs^{A549}{}_{batch}$, EVs^{A549}-coated FSNs using the discontinuous approach; $FSNs\text{-}EVs^{A549}{}_{micro}$, EVs^{A549}-coated FSNs using the microfluidic strategy.

REFERENCES

(1) Fan, D.; Cao, Y.; Cao, M.; Wang, Y.; Cao, Y.; Gong, T. Nanomedicine in cancer therapy. *Signal. Transduct. Target. Ther.* **2023**, *8*, 293.

(2) He, H.; Liu, L.; Morin, E. E.; Liu, M.; Schwendeman, A. Survey of Clinical Translation of Cancer Nanomedicines-Lessons Learned from Successes and Failures. *Acc. Chem. Res.* **2019**, *52*, 2445−2461.

(3) Đorđević, S.; Gonzalez, M. M.; Conejos-Sánchez, I.; Carreira, B.; Pozzi, S.; Acúrcio, R. C.; Satchi-Fainaro, R.; Florindo, H. F.; Vicent, M. J. Current hurdles to the translation of nanomedicines from bench to the clinic. *Drug Delivery Transl. Res.* **2022**, *12*, 500−525.

(4) Sun, D.; Zhou, S.; Gao, W. What Went Wrong with Anticancer Nanomedicine Design and How to Make It Right. *ACS Nano* **2020**, *14*, 12281−12290.

(5) Wilhelm, S.; Tavares, A. J.; Dai, Q.; Ohta, S.; Audet, J.; Dvorak, H. F.; Chan, W. C. W. Analysis of nanoparticle delivery to tumous. *Nat. Rev. Mater.* **2016**, *1*, 1604.
(6) Sancho-Albero, M.; Encinas-Giménez, M.; Sebastian, V.; Pérez, E.; Luján, L.; Santamaría, J.; Martín-Duque, P. Transfer of photothermal nanoparticles using stem cell derived small extracellular vesicles for in vivo treatment of primary and multinodular tumours. *J. Extracell. Vesicles* **2022**, *11*, No. e12193.
(7) Sancho-Albero, M.; Sebastian, V.; Perez-Lopez, A. M.; Martín-Duque, P.; Unciti-Broceta, A.; Santamaria, J. Extracellular Vesicles-Mediated Bio-Orthogonal Catalysis in Growing Tumors. *Cells* **2024**, *13*, 691.
(8) Sancho-Albero, M.; Navascués, N.; Mendoza, G.; Sebastián, V.; Arruebo, M.; Martín-Duque, P.; Santamaría, J. Exosome origin determines cell targeting and the transfer of therapeutic nanoparticles towards target cells. *J. Nanobiotechnol.* **2019**, *17*, 16.
(9) Alderton, G. K. Metastasis. Exosomes drive premetastatic niche formation. *Nat. Rev. Cancer* **2012**, *12*, 447.
(10) Giusti, I.; Poppa, G.; Di Fazio, G.; D'Ascenzo, S.; Dolo, V. Metastatic Dissemination: Role of Tumor-Derived Extracellular Vesicles and Their Use as Clinical Biomarkers. *Int. J. Mol. Sci.* **2023**, *24*, 9590.
(11) Furioso Ferreira, R.; Ghaffari, M. H.; Ceciliani, F.; Fontana, M.; Caruso, D.; Audano, M.; Savoini, G.; Agazzi, A.; Mrljak, V.; Sauerwein, H. Correction: Untargeted lipidomics reveals unique lipid signatures of extracellular vesicles from porcine colostrum and milk. *PLoS One* **2025**, *20*, No. e0326133.
(12) Rai, A.; Huynh, K.; Cross, J.; Poh, Q. H.; Fang, H.; Claridge, B.; Duong, T.; Duarte, C.; Shaw, J. E.; Marwick, T. H.; Meikle, P.; Greening, D. W. Multi-omics identify hallmark protein and lipid features of small extracellular vesicles circulating in human plasma. *Nat. Cell Biol.* **2025**, *27*, 2167−2185.
(13) Vázquez-Ríos, A. J.; Molina-Crespo, A.; Bouzo, B. L.; López-López, R.; Moreno-Bueno, G.; de la Fuente, M. Exosome-mimetic nanoplatforms for targeted cancer drug delivery. *J. Nanobiotechnol.* **2019**, *17*, 85.
(14) Zhou, X.; Miao, Y.; Wang, Y.; He, S.; Guo, L.; Mao, J.; Chen, M.; Yang, Y.; Zhang, X.; Gan, Y. Tumour-derived extracellular vesicle membrane hybrid lipid nanovesicles enhance siRNA delivery by tumour-homing and intracellular freeway transportation. *J. Extracell. Vesicles* **2022**, *11*, No. e12198.
(15) Chernyshev, V. S.; Nozdriukhin, D.; Chuprov-Netochin, R.; Tsydenzhapova, E.; Novoselova, M.; Gorin, D.; Yashchenok, A. Engineered multicompartment vesicosomes for selective uptake by living cells. *Colloids Surf., B.* **2022**, *220*, 112953.
(16) Khongkow, M.; Yata, T.; Boonrungsiman, S.; Ruktanonchai, U. R.; Graham, D.; Namdee, K. Surface modification of gold nanoparticles with neuron-targeted exosome for enhanced blood−brain barrier penetration. *Sci. Rep.* **2019**, *9*, 8278.
(17) Sancho-Albero, M.; Decio, A.; Akpinar, R.; De Luigi, A.; Giavazzi, R.; Terracciano, L.; De Cola, L. Melanoma extracellular vesicles membrane coated nanoparticles as targeted delivery carriers for tumor and lungs. *Mater. Today Bio* **2025**, *30*, 101433.
(18) Saeed, M. M.; Carthy, E.; Dunne, N.; Kinahan, D. Advances in nanoparticle synthesis assisted by microfluidics. *Lab Chip* **2025**, *25*, 3060−3093.
(19) Yao, F.; Zhu, P.; Chen, J.; Li, S.; Sun, B.; Li, Y.; Zou, M.; Qi, X.; Liang, P.; Chen, Q. Synthesis of nanoparticles via microfluidic devices and integrated applications. *Microchim. Acta* **2023**, *190*, 256.
(20) Chen, Y.; Douanne, N.; Wu, T.; Kaur, I.; Tsering, T.; Erzingatzian, A.; Nadeau, A.; Juncker, D.; Nerguizian, V.; Burnier, J. V. Leveraging nature's nanocarriers: Translating insights from extracellular vesicles to biomimetic synthetic vesicles for biomedical applications. *Sci. Adv.* **2025**, *11*, No. eads5249.
(21) Gomez, L.; Sebastian, V.; Irusta, S.; Ibarra, A.; Arruebo, M.; Santamaria, J. Scaled-up production of plasmonic nanoparticles using microfluidics: from metal precursors to functionalized and sterilized nanoparticles. *Lab Chip* **2014**, *14*, 325−332.
(22) Uson, L.; Sebastian, V.; Arruebo, M.; Santamaria, J. Continuous microfluidic synthesis and functionalization of gold nanorods. *Chem. Eng. J.* **2016**, *285*, 286−292.
(23) Hao, N.; Nie, Y.; Zhang, J. X. J. Microfluidic Flow Synthesis of Functional Mesoporous Silica Nanofibers with Tunable Aspect Ratios. *ACS Sustain. Chem. Eng.* **2018**, *6*, 1522−1526.
(24) Kašpar, O.; Koyuncu, A. H.; Hubatová-Vacková, A.; Balouch, M.; Tokárová, V. Influence of channel height on mixing efficiency and synthesis of iron oxide nanoparticles using droplet-based microfluidics. *RSC Adv.* **2020**, *10*, 15179−15189.
(25) Yolchinyan, S. A.; Hobosyan, M. A.; Martirosyan, K. S. Tailoring bismuth oxide flower-, bowtie- and brushwood-like structures through microfluidic synthesis. *Mater. Chem. Phys.* **2018**, *207*, 330−336.
(26) Wojnicki, M.; Hessel, V. Quantum materials made in microfluidics - critical review and perspective. *Chem. Eng. J.* **2022**, *438*, 135616.
(27) Mehraji, S.; DeVoe, D. L. Microfluidic synthesis of lipid-based nanoparticles for drug delivery: recent advances and opportunities. *Lab Chip* **2024**, *24*, 1154−1174.
(28) Udepurkar, A. P.; Mampaey, L.; Clasen, C.; Sebastián Cabeza, V.; Kuhn, S. Microfluidic synthesis of PLGA nanoparticles enabled by an ultrasonic microreactor. *React. Chem. Eng.* **2024**, *9*, 2208−2217.
(29) Shepherd, S. J.; Warzecha, C. C.; Yadavali, S.; El-Mayta, R.; Alameh, M.-G.; Wang, L.; Weissman, D.; Wilson, J. M.; Issadore, D.; Mitchell, M. J. Scalable mRNA and siRNA Lipid Nanoparticle Production Using a Parallelized Microfluidic Device. *Nano Lett.* **2021**, *21*, 5671−5680.
(30) Kouhkord, A.; Hassani, F.; Amirmahani, M.; Golshani, A.; Naserifar, N.; Moghanlou, F. S.; Beris, T. Controllable Microfluidic System through Intelligent Framework: Data-Driven Modeling, Machine Learning Energy Analysis, Comparative Multiobjective Optimization, and Experimental Study. *Ind. Eng. Chem. Res.* **2024**, *63*, 13326−13344.
(31) Sebastian Cabeza, V.; Kuhn, S.; Kulkarni, A. A.; Jensen, K. F. Size-Controlled Flow Synthesis of Gold Nanoparticles Using a Segmented Flow Microfluidic Platform. *Langmuir* **2012**, *28*, 7007−7013.
(32) Agha, A.; Waheed, W.; Stiharu, I.; Nerguizian, V.; Destgeer, G.; Abu-Nada, E.; Alazzam, A. A review on microfluidic-assisted nanoparticle synthesis, and their applications using multiscale simulation methods. *Discovery Nano* **2023**, *18*, 18.
(33) Garcia-Salinas, S.; Himawan, E.; Mendoza, G.; Arruebo, M.; Sebastian, V. Rapid on-Chip Assembly of Niosomes: Batch versus Continuous Flow Reactors. *ACS Appl. Mater. Interfaces* **2018**, *10*, 19197−19207.
(34) Molinaro, R.; Evangelopoulos, M.; Hoffman, J.; Corbo, C.; Taraballi, F.; Martinez, J. O.; Hartman, K. A.; Cosco, D.; Costa, G.; Romeo, I.; Sherman, M.; Paolino, D.; Alcaro, S.; Tasciotti, E. Design and Development of Biomimetic Nanovesicles Using a Microfluidic Approach. *Adv. Mater.* **2018**, *30*, No. e1702749.
(35) Zhang, L.; Feng, Q.; Wang, J.; Zhang, S.; Ding, B.; Wei, Y.; Dong, M.; Ryu, J.-Y.; Yoon, T.-Y.; Shi, X.; Sun, J.; Jiang, X. Microfluidic Synthesis of Hybrid Nanoparticles with Controlled Lipid Layers: Understanding Flexibility-Regulated Cell-Nanoparticle Interaction. *ACS Nano* **2015**, *9*, 9912−9921.
(36) Feng, Q.; Zhang, L.; Liu, C.; Li, X.; Hu, G.; Sun, J.; Jiang, X. Microfluidic based high throughput synthesis of lipid-polymer hybrid nanoparticles with tunable diameters. *Biomicrofluidics* **2015**, *9*, 052604.
(37) Liu, C.; Zhang, W.; Li, Y.; Chang, J.; Tian, J.; Zhao, F.; Ma, Y.; Sun, J. Microfluidic Sonication to Assemble Exosome Membrane-Coated Nanoparticles for Immune Evasion-Mediated Targeting. *Nano Lett.* **2019**, *19*, 7836−7844.
(38) Cardellini, J.; Normak, K.; Gerlt, M.; Makasewicz, K.; Seiffert, C.; Capasso Palmiero, U.; Ye, S.; González Gómez, M. A.; Piñero, Y.; Rivas, J.; Bongiovanni, A.; Bergese, P.; Arosio, P. Microfluidics-Driven Manufacturing and Multiscale Analytical Characterization of Nanoparticle-Vesicle Hybrids. *Adv. Healthc. Mater.* **2025**, *14*, 2403264.

https://doi.org/10.1021/acsanm.5c05265
ACS Appl. Nano Mater. XXXX, XXX, XXX−XXX

(39) Pareja Tello, R.; Lamparelli, E. P.; Ciardulli, M. C.; Hirvonen, J.; Barreto, G.; Mafulli, N.; Della Porta, G.; Santos, H. A. Hybrid lipid nanoparticles derived from human mesenchymal stem cell extracellular vesicles by microfluidic sonication for collagen I mRNA delivery to human tendon progenitor stem cells. *Biomater. Sci.* **2025**, *13*, 2066−2081.
(40) Cheng, G.; Li, W.; Ha, L.; Han, X.; Hao, S.; Wan, Y.; Wang, Z.; Dong, F.; Zou, X.; Mao, Y.; Zheng, S. Y. Self-Assembly of Extracellular Vesicle-like Metal-Organic Framework Nanoparticles for Protection and Intracellular Delivery of Biofunctional Proteins. *J. Am. Chem. Soc.* **2018**, *140*, 7282−7291.
(41) Lee, J.-R.; Park, B.-W.; Kim, J.; Choo, Y. W.; Kim, H. Y.; Yoon, J.-K.; Kim, H.; Hwang, J.-W.; Kang, M.; Kwon, S. P.; Song, S. Y.; Ko, I. O.; Park, J.-A.; Ban, K.; Hyeon, T.; Park, H. J.; Kim, B.-S. Nanovesicles derived from iron oxide nanoparticles-incorporated mesenchymal stem cells for cardiac repair. *Sci. Adv.* **2020**, *6*, No. eaaz0952.
(42) Zhang, J.; Ji, C.; Zhang, H.; Shi, H.; Mao, F.; Qian, H.; Xu, W.; Wang, D.; Pan, J.; Fang, X.; Santos, H. A.; Zhang, X. Engineered neutrophil-derived exosome-like vesicles for targeted cancer therapy. *Sci. Adv.* **2022**, *8*, No. eabj8207.
(43) Stöber, W.; Fink, A.; Bohn, E. Controlled growth of monodisperse silica spheres in the micron size range. *J. Colloid Interface Sci.* **1968**, *26*, 62−69.
(44) Clemente, A.; Moreno, N.; Lobera, M. P.; Balas, F.; Santamaria, J. Versatile hollow fluorescent metal-silica nanohybrids through a modified microemulsion synthesis route. *J. Colloid Interface Sci.* **2018**, *513*, 497−504.
(45) Sancho-Albero, M.; Rubio-Ruiz, B.; Pérez-López, A. M.; Sebastián, V.; Martín-Duque, P.; Arruebo, M.; Santamaría, J.; Unciti-Broceta, A. Cancer-derived exosomes loaded with ultrathin palladium nanosheets for targeted bioorthogonal catalysis. *Nat. Catal.* **2019**, *2*, 864−872.
(46) Arruebo, M.; Uson, L.; Miana, M.; Ortiz de Solorzano, I.; Sebastian, V.; Larrea, A. Continuous synthesis of drug-loaded nanoparticles using microchannel emulsification and numerical modeling: effect of passive mixing. *Int. J. Nanomed.* **2016**, *11*, 3397−3416.
(47) Bryantsev, V. S.; Diallo, M. S.; Goddard, W. A. pKa Calculations of Aliphatic Amines, Diamines, and Aminoamides via Density Functional Theory with a Poisson−Boltzmann Continuum Solvent Model. *J. Phys. Chem. A* **2007**, *111*, 4422−4430.
(48) Liu, L.; Bai, X.; Martikainen, M.-V.; Karlund, A.; Roponen, M.; Xu, W.; Hu, G.; Tasciotti, E.; Lehto, V.-P. Cell membrane coating integrity affects the internalization mechanism of biomimetic nanoparticles. *Nat. Commun.* **2021**, *12*, 5726.
(49) Desai, N.; Tambe, V.; Pofali, P.; Vora, L. K. Cell Membrane-Coated Nanoparticles: A New Frontier in Immunomodulation. *Adv. NanoBiomed Res.* **2024**, *4*, 2400012.
(50) Graván, P.; Marchal, J. A.; Galisteo-González, F. Improving tumor treatment: Cell membrane-coated nanoparticles for targeted therapies. *Mater. Today Bio* **2025**, *32*, 101716.
(51) Zhou, Z.; Zhang, S.; Xue, N. Research progress of cancer cell membrane coated nanoparticles for the diagnosis and therapy of breast cancer. *Front. Oncol.* **2023**, *13*, 1270407.
(52) Lorencova, L.; Bertok, T.; Bertokova, A.; Gajdosova, V.; Hroncekova, S.; Vikartovska, A.; Kasak, P.; Tkac, J. Exosomes as a Source of Cancer Biomarkers: Advances in Electrochemical Biosensing of Exosomes. *ChemElectroChem* **2020**, *7*, 1956−1973.
(53) Welsh, J. A.; Goberdhan, D. C. I.; O'Driscoll, L.; Buzas, E. I.; Blenkiron, C.; Bussolati, B.; Cai, H.; Di Vizio, D.; Driedonks, T. A. P.; Erdbrügger, U.; Falcon-Perez, J. M.; Fu, Q.-L.; Hill, A. F.; Lenassi, M.; Lim, S. K.; Mahoney, M. G.; Mohanty, S.; Möller, A.; Nieuwland, R.; Ochiya, T.; Sahoo, S.; Torrecilhas, A. C.; Zheng, L.; Zijlstra, A.; Abuelreich, S.; Bagabas, R.; Bergese, P.; Bridges, E. M.; Brucale, M.; Burger, D.; Carney, R. P.; Cocucci, E.; Crescitelli, R.; Hanser, E.; Harris, A. L.; Haughey, N. J.; Hendrix, A.; Ivanov, A. R.; Jovanovic-Talisman, T.; Kruh-Garcia, N. A.; Ku'ulei-Lyn Faustino, V.; Kyburz, D.; Lässer, C.; Lennon, K. M.; Lötvall, J.; Maddox, A. L.; Martens-Uzunova, E. S.; Mizenko, R. R.; Newman, L. A.; Ridolfi, A.; Rohde, E.; Rojalin, T.; Rowland, A.; Saftics, A.; Sandau, U. S.; Saugstad, J. A.; Shekari, F.; Swift, S.; Ter-Ovanesyan, D.; Tosar, J. P.; Useckaite, Z.; Valle, F.; Varga, Z.; van der Pol, E.; van Herwijnen, M. J. C.; Wauben, M. H. M.; Wehman, A. M.; Williams, S.; Zendrini, A.; Zimmerman, A. J.; ThéryWitwer, C. K. W.; Théry, C.; Witwe, K. W. Minimal information for studies of extracellular vesicles (MISEV2023): From basic to advanced approaches. *J. Extracell. Vesicles* **2024**, *13*, No. e12404.
(54) Wiklander, O. P. B.; Bostancioglu, R. B.; Welsh, J. A.; Zickler, A. M.; Murke, F.; Corso, G.; Felldin, U.; Hagey, D. W.; Evertsson, B.; Liang, X.-M.; Gustafsson, M. O.; Mohammad, D. K.; Wiek, C.; Hanenberg, H.; Bremer, M.; Gupta, D.; Bjornstedt, M.; Giebel, B.; Nordin, J. Z.; Jones, J. C.; El Andaloussi, S.; Görgens, A. Systematic Methodological Evaluation of a Multiplex Bead-Based Flow Cytometry Assay for Detection of Extracellular Vesicle Surface Signatures. *Front. Immunol.* **2018**, *9*, 1326.
(55) Tsui, F. C.; Ojcius, D. M.; Hubbell, W. L. The intrinsic pKa values for phosphatidylserine and phosphatidylethanolamine in phosphatidylcholine host bilayers. *Biophys. J.* **1986**, *49*, 459−468.
(56) Issa, A. A.; El-Azazy, M.; Luyt, A. S. Kinetics of alkoxysilanes hydrolysis: An empirical approach. *Sci. Rep.* **2019**, *9*, 17624.
(57) Barry, E.; Dogic, Z. Entropy driven self-assembly of nonamphiphilic colloidal membranes. *Proc. Natl. Acad. Sci. U S A* **2010**, *107*, 10348−10353.
(58) Sadeghi, M. Investigating the entropic nature of membrane-mediated interactions driving the aggregation of peripheral proteins. *Soft Matter* **2022**, *18*, 3917−3927.
(59) Nzai, J. M.; Proctor, A. Determination of phospholipids in vegetable oil by fourier transform infrared spectroscopy. *J. Am. Oil Chem. Soc.* **1998**, *75*, 1281−1289.
(60) Chen, X.; Zou, L.-Q.; Niu, J.; Liu, W.; Peng, S.-F.; Liu, C.-M. The Stability, Sustained Release and Cellular Antioxidant Activity of Curcumin Nanoliposomes. *Molecules* **2015**, *20*, 14293−14311.
(61) Lewis, R. N. A. H.; McElhaney, R. N. Fourier Transform Infrared Spectroscopy in the Study of Lipid Phase Transitions in Model and Biological Membranes: practical considerations. *Methods Mol. Biol.* **2007**, *400*, 207−226.
(62) Wong, P. T. T.; Papavassiliou, E. D.; Rigas, B. Phosphodiester Stretching Bands in the Infrared Spectra of Human Tissues and Cultured Cells. *Appl. Spectrosc.* **1991**, *45*, 1563−1567.
(63) Tarn, D.; Ashley, C. E.; Xue, M.; Carnes, E. C.; Zink, J. I.; Brinker, J. Mesoporous silica nanoparticle nanocarriers: biofunctionality and biocompatibility. *Acc. Chem. Res.* **2013**, *46*, 792−801.
(64) Tang, F.; Li, L.; Chen, D. Mesoporous silica nanoparticles: synthesis, biocompatibility and drug delivery. *Adv. Mater.* **2012**, *24*, 1504−1534.
(65) Huang, X.; Li, L.; Liu, T.; Hao, N.; Liu, H.; Chen, D.; Tang, F. The shape effect of mesoporous silica nanoparticles on biodistribution, clearance, and biocompatibility in vivo. *ACS Nano* **2011**, *5*, 5390−5399.
(66) Öztürk, K.; Kaplan, M.; Çalış, S. Effects of nanoparticle size, shape, and zeta potential on drug delivery. *Int. J. Pharm.* **2024**, *666*, 124799.
(67) Augustine, R.; Serpooshan, V.; Tao, W.; Hamaly, M. A.; Alkawareek, M. Y.; Dreaden, E. C.; Brown, D.; Alkilany, A. M.; Farokhzad, O.; Mahmoudi, M. Cellular uptake and retention of nanoparticles: Insights on particle properties and interaction with cellular components. *Mater. Today Commun.* **2020**, *25*, 101692.
(68) Rosso, G.; Van Veen, S. M. A.; Sancho-Albero, M.; Tamboia, G.; Empereur-Mot, C.; Perego, C.; Kuipers, M. E.; Dumontel, B.; Ajó, A.; Nolte-'t Hoen, E. N.; Pavan, G. M.; Cola, L. D.; Albertazzi, L.; Cauda, V. Rational Design of EV-Mimicking Nanoparticles with Polarity-Based Recognition Potential for Advanced Nanocarrier Development. *ACS Appl. Nano Mater.* **2025**, *8*, 13257−13273.
(69) Li, H.; Li, S.; Lin, Y.; Chen, S.; Yang, L.; Huang, X.; Wang, H.; Yu, X.; Zhang, L. Artificial exosomes mediated spatiotemporal-resolved and targeted delivery of epigenetic inhibitors. *J. Nanobiotechnol.* **2021**, *19*, 364.

https://doi.org/10.1021/acsanm.5c05265
ACS Appl. Nano Mater. XXXX, XXX, XXX−XXX

(70) Dumontel, B.; Jiménez-Jiménez, C.; Vallet-Regí, M.; Manzano, M. Bioinspired extracellular vesicle-coated silica nanoparticles as selective delivery systems. *Mater. Today Bio* **2023**, *23*, 100850.

https://doi.org/10.1021/acsanm.5c05265
ACS Appl. Nano Mater. XXXX, XXX, XXX−XXX